This article was downloaded by:
On: *25 January 2011*
Access details: *Access Details: Free Access*
Publisher *Taylor & Francis*
Informa Ltd Registered in England and Wales Registered Number: 1072954 Registered office: Mortimer House, 37-41 Mortimer Street, London W1T 3JH, UK

Liquid Crystals

Publication details, including instructions for authors and subscription information:
http://www.informaworld.com/smpp/title~content=t713926090

A numerical technique for predicting microstructure in liquid crystalline polymers

John Hobdell; Alan Windle

Online publication date: 06 August 2010

To cite this Article Hobdell, John and Windle, Alan(1997) 'A numerical technique for predicting microstructure in liquid crystalline polymers', Liquid Crystals, 23: 2, 157 — 173

To link to this Article: DOI: 10.1080/026782997208415

URL: http://dx.doi.org/10.1080/026782997208415

PLEASE SCROLL DOWN FOR ARTICLE

Full terms and conditions of use: http://www.informaworld.com/terms-and-conditions-of-access.pdf

This article may be used for research, teaching and private study purposes. Any substantial or systematic reproduction, re-distribution, re-selling, loan or sub-licensing, systematic supply or distribution in any form to anyone is expressly forbidden.

The publisher does not give any warranty express or implied or make any representation that the contents will be complete or accurate or up to date. The accuracy of any instructions, formulae and drug doses should be independently verified with primary sources. The publisher shall not be liable for any loss, actions, claims, proceedings, demand or costs or damages whatsoever or howsoever caused arising directly or indirectly in connection with or arising out of the use of this material.

LIQUID CRYSTALS, 1997, VOL. 23, NO. 2, 157–173

A numerical technique for predicting microstructure in liquid crystalline polymers

by JOHN HOBDELL and ALAN WINDLE*

Department of Materials Science and Metallurgy, Cambridge University,
Pembroke Street, Cambridge CB2 3QZ, U.K.

(*Received 9 December 1996; accepted 7 March 1997*)

A numerical technique has been developed to model texture in nematic liquid crystals. The technique differentiates between splay, twist and bend distortions and includes splay–splay compensation. The technique is tested by the simulation of the Fréedericksz transition and by the determination of minimum energy director fields for specific boundary conditions. To model the bulk, periodic boundary conditions are imposed. The effect of elastic anisotropy on disclination character has been investigated by terminating simulations before all the defects have been annihilated. With a low twist constant, twist disclinations are observed; with a high twist constant, wedge disclinations are observed. With a low twist constant and high splay constant, realistic for polymeric liquid crystals, features observed experimentally are simulated.

1. Introduction

Thermotropic liquid crystalline polymers (TLCPs) have great potential as structural materials. They have high strength and stiffness in the direction of molecular alignment and their low melt viscosity facilitates processing [1]. Without resort to large aligning fields, moulded samples show inhomogeneities either in the form of variations in the direction of alignment across the sample or as topological defects. An understanding of such features is crucial to the further utilization of these promising materials.

The simplest type of liquid crystals are nematic liquid crystals. In the nematic mesophase, the molecules exhibit long range orientational order without any long range translational order; the molecules tend to align, but their centres of mass do not lie on a regular lattice. The mean molecular orientation can be described by a uniaxial tensor termed the 'director'. At larger size scales the orientation of the director itself may vary and it is such variations which appear as microstructural textures and defects.

The elastic theory of curvature distortions was developed by Oseen [2] and Frank [3]. In the absence of an applied orienting field, the free-energy density is given by equation (1).

$$F=\frac{1}{2}[k_{11}(\nabla\,\mathbf{n})^2+k_{22}(\mathbf{n}\;\nabla\wedge\mathbf{n})^2+k_{33}(\mathbf{n}\wedge\nabla\wedge\mathbf{n})^2] \qquad (1)$$

where $\mathbf{n}$ is a unit vector parallel everywhere to the director field and k_{11}, k_{22} and k_{33} are the three Frank elastic constants associated with splay, twist and bend distortions, respectively.

In small molecule nematics, the elastic constants are often taken to be equal, allowing a significant simplification of equation (1). In polymeric nematics this is not a reasonable assumption. In TLCPs, the splay constant is the highest of the three elastic constants and the twist constant is the lowest. The splay constant is large in semi-flexible polymeric nematics because splay distortion requires a segregation of chain ends. For a long chain molecule there are very few chain ends per unit volume and so the very particular organization of chain ends necessary to allow any splay distortion is entropically unfavourable [4]. Recent experimental studies have suggested that there may be as much as a factor of ten difference between the splay and bend constants and the bend and twist constants in some TLCPs [5]. In addition to the splay, twist and bend elastic constants, two other elastic constants exist, k_{13} and k_{24}. This paper will deal primarily with the first three elastic constants, but the implications of the k_{24}, or 'saddle-splay', constant will be explored.

In order to probe the effect of unequal elastic constants on microstructural defects and textures we have developed a numerical technique which forms the basis of this paper which is arranged as follows. Section 2 presents details of the numerical technique itself; §3 shows tests of the technique against analytical results (where these are available); §4 presents the results of

*Author for correspondence.

simulations, and their comparison with experiment, and §5 is a discussion of the results.

2. Numerical technique

Several workers have developed mesoscale methods for simulating texture and texture evolution in liquid crystals. These methods have either relied on the equal constant approximation [6–8], have been restricted to two dimensions [9] or have adopted both limitations [10] and none has addressed the issue of splay–splay compensation where splay on one plane is opposite to splay on a perpendicular plane [4]. In order to simulate polymeric nematics in three dimensions, it is necessary to distinguish between the three types of distortion in three dimensions. The method we have adopted involves dividing the geometry of interest into an array of cubic cells, as shown in figure 1. Each cell stores a director to represent the local orientation. Since the materials are deep in the nematic phase, the local order parameter is considered to be fixed and the local director is stored as a vector whose direction is parallel to the local orientation. Clearly a vector does not have the correct uniaxial symmetry for a nematic director, which is technically a tensor, and this complication is overcome in the calculation of the distortion energy described later.

2.1. *Program structure*

The first stage is to initialize the model. Either the directors are all aligned to simulate a monodomain or set to random orientations to simulate an isotropic condition. Directors in cells forming the boundaries are fixed at specific orientations, usually either parallel to the boundary to simulate planar boundary conditions or perpendicular to the boundary to simulate homeotropic boundary conditions. Periodic boundary conditions may also be simulated by considering the cells down one face of the model to have the cells on the opposite face of the model as their external neighbours.

Following initialization, an annealing algorithm is used to reduce the total energy of the system. It involves picking cells at random and assigning a randomly chosen trial orientation to the director stored therein. The difference in the total system energy between the existing orientation and the trial orientation is found using the energy calculation described in §2.2. A Metropolis [11] algorithm is used to decide whether to accept or reject the trial orientation. If the energy with the trial orientation is lower than that calculated with the existing orientation, then the trial orientation is accepted. If, however, the energy with the trial orientation is higher than that with the existing orientation, then the new trial orientation is accepted with a probability given by equation (2).

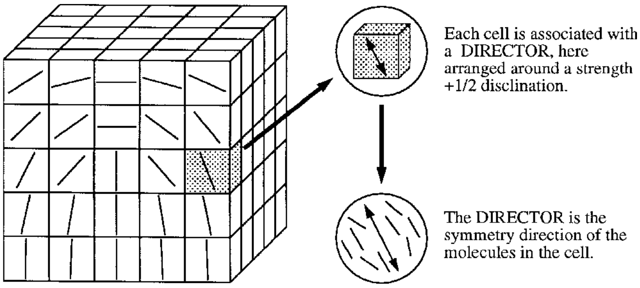

Figure 1. The model. Each cubic cell stores a director which is parallel to the average orientation of the long axes of the molecules within the cell.

$$P = \exp[-\beta(E_{\mathrm{trial}} - E_{\mathrm{old}})] \tag{2}$$

In equation (2), $\beta = 1/kT$, where k is the Boltzmann constant and T is the 'temperature'. The 'temperature' in this case is not the thermodynamic temperature but is part of the numerical technique. The technique may be used in two modes. If the global minimum is sought, then the 'temperature' is gradually lowered from a high value towards zero. The effect of an elevated 'temperature' is to allow the system to climb out of local minima. However, too high a 'temperature' will mean the system is near to a nematic–isotropic transition where it ceases to be a reasonable assumption to have a fixed order parameter and there is a high degree of fluctuation in the orientations of the directors.

As the system tends towards a minimum more and more of the trial orientations are rejected and there is a tendency for the algorithm to become very inefficient. The ratio of accepted changes to trials is termed the acceptance ratio. In order to increase the acceptance ratio it is necessary to reduce the angular variation of the trial orientations. It is a simple matter to define a cone of semi-angle γ about the current director orientation and select a trial orientation with a uniform probability from within this cone. The smaller the semi-angle, γ, the higher the probability of acceptance. An acceptance ratio of 50 per cent is widely chosen (for a discussion of this see [12]) and to maintain this value a feedback mechanism is included. The acceptance ratio is calculated every 500 trials and the cone semi-angle is altered according to the scheme in equation (3).

$$\gamma_{\mathrm{new}} = \frac{\text{Calculated acceptance ratio}}{\text{Required acceptance ratio}}\,\gamma \tag{3}$$

An additional check ensures that the cone semi-angle does not vary by more than a factor of 10 after any one set of 500 trials.

The second mode of running the simulations is to fix the 'temperature' at a value well below the nematic–isotropic transition and to select every new trial orientation from an isotropic distribution. Simulations are run from a randomized initial state with periodic boundary conditions allowing the evolution of textures via the annihilation of defects. It is possible to examine the character of the defects which occur during the evolution as a function of the elastic constants. For these simulations, the effect of the Metropolis algorithm is to apply a fluctuation to the directors to aid the annealing process. It is, in effect, a low 'temperature' Monte Carlo simulation.

The question of the size of the cells is of some importance. As will be shown later, the model accurately reproduces continuum results. When simulations are annealed to the minimum energy state, at zero Monte Carlo temperature, the results are in the continuum limit and increasing the number of cells merely increases the resolution. If the Monte Carlo temperature is not zero, then the simulations will include the effect of thermal fluctuations. In the simulations presented here, all the results are produced with a very low Monte Carlo temperature and the effect of the fluctuations is very small. Such small fluctuations are included purely to prevent simulations locking-up in local minima.

There is a relationship between the size of the cells and the Monte Carlo temperature. If the cells are of molecular scale, then the technique may be used to simulate a nematic–isotropic transition in much the same way as Lebwohl and Lasher did [13]. At this size scale the interaction energy must be considered in terms of an intermolecular potential rather than a distortion free energy. If the cell size is increased, then each cell may be considered to contain more than a single molecule and the effect of thermal fluctuations (at the same value of kT per cell) will be reduced. As the size of each cell is increased further, the effect of thermal fluctuations is reduced and the system will tend towards the continuum limit where thermal fluctuations are negligible. For a given distortion, the distortion free energy scales linearly with the distance across which the distortion occurs. This statement implies that the coefficient, β, in equation (2) may be interpreted either as a reciprocal temperature or as a size scale. In this work we consider values of β which are large and interpret this to be a large size scale, approaching the continuum limit. In future work the effect of smaller values of β will be considered as a way of bridging the gap between atomistic and continuum size scales.

2.2. *Energy calculation*

The calculation of the energy is based on Frank's equation (equation (1)) for the free energy associated with a distorted director field, **n**, in a liquid crystal. By basing the calculation on this equation it is possible to separate the contributions from splay, twist and bend distortions. The equation is expanded into a set of partial derivatives as shown in equations (4) to (6).

$$(\nabla \mathbf{n})^2=\left(\frac{\partial n_x}{\partial x}+\frac{\partial n_y}{\partial y}+\frac{\partial n_z}{\partial z}\right)^2 \tag{4}$$

$$[\mathbf{n}\ (\nabla\wedge\mathbf{n}]^2=\left[n_x\left(\frac{\partial n_z}{\partial y}-\frac{\partial n_y}{\partial z}\right)+n_y\left(\frac{\partial n_x}{\partial z}-\frac{\partial n_z}{\partial x}\right)+n_z\left(\frac{\partial n_y}{\partial x}-\frac{\partial n_x}{\partial y}\right)\right]^2 \tag{5}$$

$$\begin{aligned}(\mathbf{n}\wedge(\nabla\wedge\mathbf{n}))^2=\Bigg| & i\left[n_y\left(\frac{\partial n_y}{\partial x}-\frac{\partial n_x}{\partial y}\right)-n_z\left(\frac{\partial n_x}{\partial z}-\frac{\partial n_z}{\partial x}\right)\right]\\ & +j\left[n_z\left(\frac{\partial n_z}{\partial y}-\frac{\partial n_y}{\partial z}\right)-n_x\left(\frac{\partial n_y}{\partial x}-\frac{\partial n_x}{\partial y}\right)\right]\\ & +k\left[n_x\left(\frac{\partial n_x}{\partial z}-\frac{\partial n_z}{\partial x}\right)-n_y\left(\frac{\partial n_z}{\partial y}-\frac{\partial n_y}{\partial z}\right)\right]\Bigg|^2\end{aligned} \tag{6}$$

Note that equations (4) and (5) are scalar and the result may simply be squared to give the distortion to insert into equation (1), while equation (6) produces a vector and it is its magnitude squared that is inserted into equation (1).

The energy is calculated for a single cell. Firstly, the cell is broken down into eight corners. Around each corner are three neighbours as shown in figure 2. For each corner, the three neighbours are used to calculate values for the splay, twist and bend distortions by approximating the partial derivatives by forward differences. For example, the change in the x component of the director with respect to x is given by equation (7):

$$\frac{\partial n_x}{\partial x}=\frac{n_x(i+1,j,k)-n_x(i,j,k)}{\Delta L} \tag{7}$$

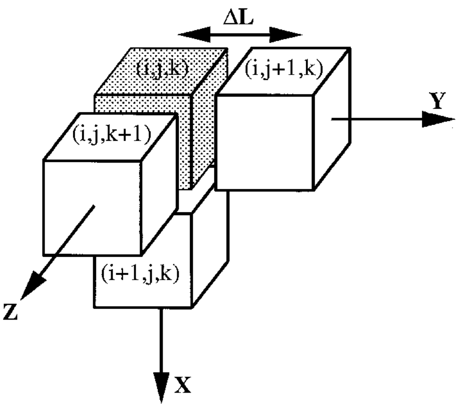

Figure 2. Around each cell there are eight corners; around each corner are three neighbouring cells. In the diagram, the three neighbours shown are along the positive coordinate axes.

The change in the y component of the director with respect to z is given by equation (8):

$$\frac{\partial n_y}{\partial z}=\frac{n_y(i,j,k+1)-n_y(i,j,k)}{\Delta L} \tag{8}$$

The other seven partial derivatives found in equations (4) to (6) are approximated similarly.

It is necessary to use forward differences rather than central differences since it is a requirement of the algorithm to have a dependence on the orientation of the director stored in the central cell. In central differences, the derivative at a point is given by the difference between the value in the cell to the left and the value in the cell to the right. In the approach adopted here, the derivative is approximated by the difference between the cell to one side and the central cell. In order to ensure that cells to both sides of the central cell have equal weighting, splay, twist and bend distortions are calculated for all eight sets of three neighbours around the corners of the central cell and the eight values are averaged. Energies are obtained by multiplying each distortion by the relevant elastic constant.

On changing the orientation of the central director, the energies calculated for the six nearest neighbours will change. In order to calculate the change in the *system* energy as a result of changing the orientation of a single director it is necessary to recalculate all terms which include the orientation of that director. In fact this involves recalculating all eight corners of the central cell and four of the corners of each of the six neighbouring cells.

One complication is the inability of vectors to describe nematic symmetry. This is dealt with by inserting a simple check to determine whether two vectors make an acute angle with each other or not. If the angle is greater than 90° then one of the vectors is flipped through 180° so that the angle is less than 90°. This does give a discontinuity in the gradient of the energy function whenever neighbours are at 90° to each other, but since this will only happen at the cores of disclinations where low angle elasticity is inapplicable anyway, it is accepted in this work.

An alternative way of dealing with the problem of the nematic symmetry is to describe the director by a second rank tensor rather than a vector. This approach has been used by the authors [14] with only splay distortion considered and, more recently, by Gruhn and Hess [15]. These workers have presented an elegant Monte Carlo algorithm which distinguishes between the three elastic constants with a tensor description of the director field. Although their description eliminates the need for the flipping algorithm utilized in this work and is, in principle, extendable to three dimensions, Gruhn and Hess have only presented results for two dimensional simulations.

2.3. *Splay–splay compensation and* k_{24}

One of the important advances of the method presented here is the correct handling of splay–splay compensation (figure 3). Splay distortion is described mathematically by the divergence term in Frank's equation. If the divergence of the director field on one plane is in the opposite direction to a divergence of similar magnitude on a perpendicular plane then the total divergence will be zero. This situation is known as splay–splay compensation. Previous techniques have not dealt with splay–splay compensation because only pairwise interactions between neighbours have been considered. For example the $\sin^2\theta$ algorithm used by Bedford *et al.* [16] calculated the angular difference between a central director and its six neighbours individually. The sines of the angular differences were

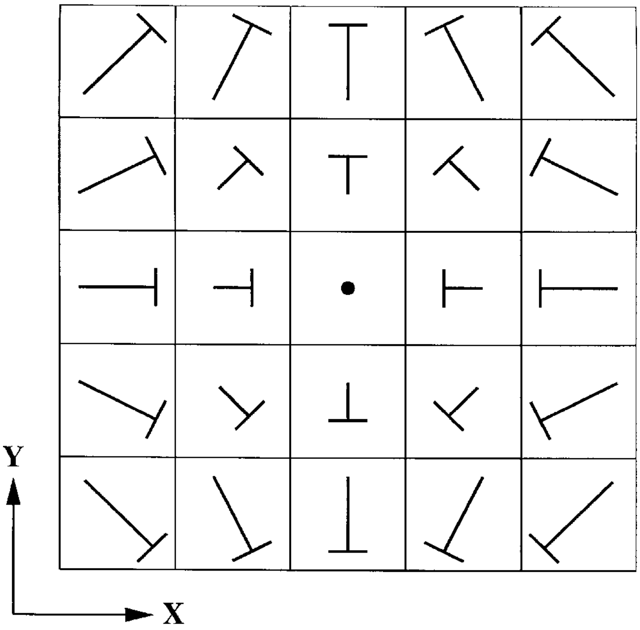

Figure 3. The diagram shows the director field for an idealised escaped −1 disclination line. The nail convention is used to represent directors pointing out of the plane. The points of the nails point out of the plane and the lengths of the shafts represents the components of the directors lying in the plane of the page. The centre of the diagram is a region of splay–splay compensation; the director field in the x-z plane splays outwards while the director field in the y-z plane splays inwards. The centre of the diagram is also a region of opposing twist distortions: along the line $x=y$ the twist is in a clockwise sense while along the line $x=-y$ the twist is in an anti-clockwise sense. Calculations for this idealized geometry show that the splay, twist and bend distortions are all zero at the centre of the diagram but that the saddle-splay distortion takes its largest value there.

found and squared before the contributions from each of the six neighbours were added. The result was that a splay–splay compensated region would have the same energy calculated as an equivalent pure splay situation where all the divergence was in the same direction.

An example of a splay–splay compensated structure is shown in figure 13. It is in fact a cross-section of an idealized escaped -1 line disclination. Calculations show that the centre of such a linear texture exhibits zero splay distortion since it is splay–splay compensated, it also exhibits zero twist distortion. However, the centre of the escaped -1 line is clearly not a region of zero distortion and the distortion in this situation is accounted for by the inclusion of the saddle-splay or k_{24} term (equation (9)) in Frank's equation (equation (1)).

$$F_{\text{saddle–splay}} = -\frac{1}{2}k_{24}[\nabla(\mathbf{n}\times\nabla\times\mathbf{n}+\mathbf{n}\nabla\,\mathbf{n})] \tag{9}$$

Although this term is often neglected it may be important in some situations. In polymeric nematics, where splay distortion is prohibited by the lack of chain ends, saddle-splay distortion may be the only way that any divergence can be accommodated. In the work presented here we have not included the k_{24} term, so perfectly splay–splay compensated geometries will have zero energy associated with them. Nevertheless, the model does have the facility for including this term and its role will be examined in future studies.

3. Testing the technique

In order to have any confidence in predictions made using this technique, a number of tests have been performed. This section describes testing of the method for special situations where the component distortions may be calculated analytically and for geometries where the minimum energy director fields are known for different sets of elastic constants.

3.1. *Energies of point defects*

A suitable set of geometries, used to test the calculation of the component distortions, was the range of Poincaré point defects [17, 18] shown in figure 4. These were chosen for a number of reasons. Firstly, analytical values of the energies may be calculated for each geometry. Secondly, the different defects all have very different amounts of splay, twist and bend distortion associated with them. Finally, the Col defect (sometimes referred to as the Hyperbolic Hedgehog) has a region of complete splay–splay compensation around its equatorial plane and so the correct determination of its energy implies the correct inclusion of splay–splay compensation in the calculations.

Table 1 shows a comparison of the energy values calculated for the model using a lattice of size 100^3. The energy of each of the defects is calculated for a spherical volume of radius R and is expressed in terms of this radius and the elastic constants. For example the analytical value for the distortion energy of a Noeud (or Hedgehog) point defect is given by:

$$E_{\text{Noeud}} = 8\pi k_{11} R \tag{10}$$

The energy for a Col (or Hyperbolic Hedgehog) is

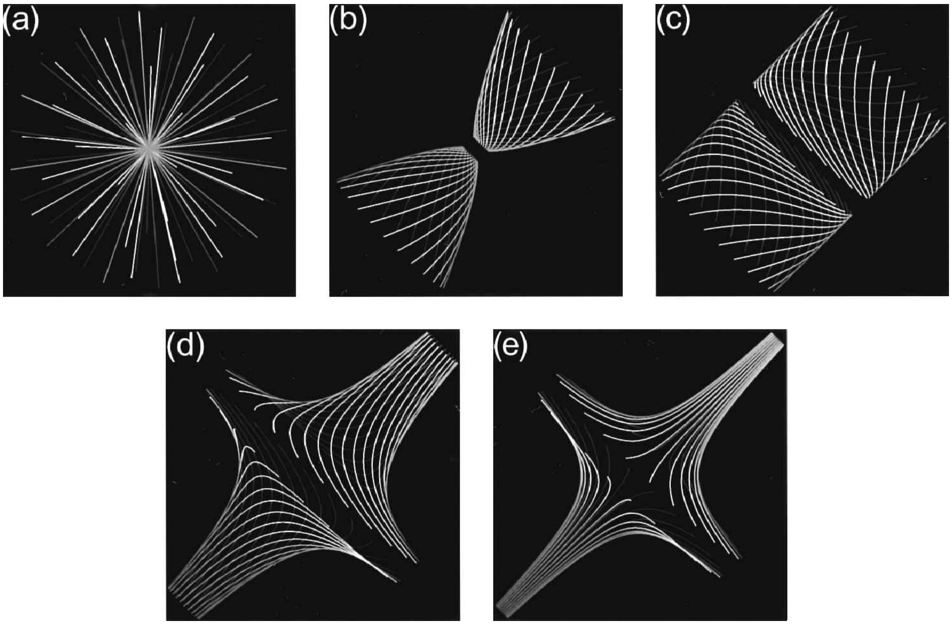

Figure 4. The range of Poincaré point defects. The director fields are illustrated by streamlines which are parallel to the director; for clarity, only a selection of the streamlines is shown. Each diagram is set with the rotational symmetry axis of the defect lying approximately from the bottom left to the top right. The equatorial plane is perpendicular to this. (*a*) The Hedgehog or Noeud point; (*b*) the Foyer point; (*c*) the Centre point; (*d*) the Col-foyer point; (*e*) the Col point.

Table 1. Energies of point defects.

	Analytical energy				Modelled energy			
Point	Splay $k_{11}R$	Twist $k_{22}R$	Bend $k_{33}R$	Total	Splay $k_{11}R$	Twist $k_{22}R$	Bend $k_{33}R$	Total
Col	5·027	0·000	3·351	8·378	5·042	0·000	3·322	8·365
Col-foyer	2·107	4·189	4·536	10·831	2·113	4·166	4·576	10·854
Centre	3·351	8·378	5·027	16·755	3·384	8·331	5·149	16·864
Foyer	16·324	4·189	2·166	22·679	16·455	4·166	2·254	22·874
Noeud	25·133	0·000	0·000	25·133	25·325	0·000	0·039	25·364

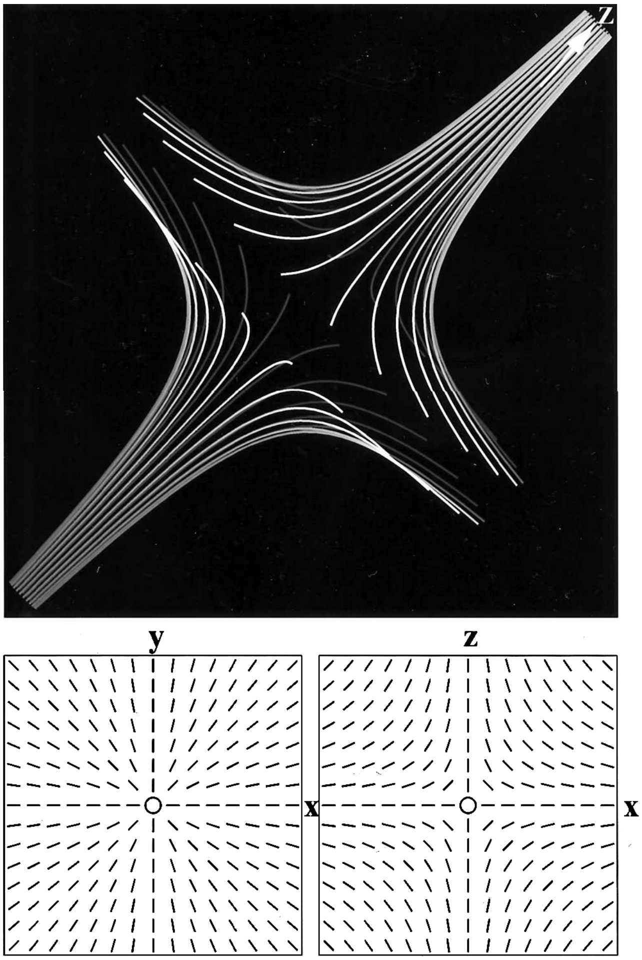

Figure 5. A Col type point defect. The streamlines in the main diagram follow the director trajectory. The inset diagrams show the director fields on the equatorial plane and on a perpendicular vertical plane. As can be seen, the divergence on the equatorial plane is away from the centre while the divergence on the vertical plane is towards the centre; the equatorial plane is thus a region which exhibits splay–splay compensation.

given by:

$$E_{\mathrm{Col}} = 8\pi R\left(\frac{k_{11}}{5} + \frac{2k_{33}}{15}\right) \qquad (11)$$

Of particular note is the correct calculation of the energy of the Col point defect. This defect contains a region of splay–splay compensation around its equatorial plane. Figure 5 shows a diagram of a Col point defect. In the x-y plane of the defect the divergence of the director field is directed outwards, but along the x axis of the x-z plane the divergence is inwards. The equatorial (x-y) plane is thus a region which exhibits splay–splay compensation. Nevertheless, the energy calculated using the new algorithm is correct and agrees with the analytical result, confirming that the model handles correctly this aspect of the distortion field.

3.2. *Parallel plates simulations*

For the modelling technique to have any useful predictive value it must be capable of finding director fields which minimize the Frank free energy. This is a variational problem and the usual approach to finding such minima is to solve the Euler–Lagrange equation for the geometry of interest. The literature contains a few examples of situations where the Euler–Lagrange equation has been solved with differing elastic constants, and comparison with these has been used as a further test of the numerical technique presented here.

One particular example for which analytical solutions were presented by Meyer [4] is shown in figure 6. The geometry is that of two parallel plates with homeotropic boundary conditions at one plate and homogeneous

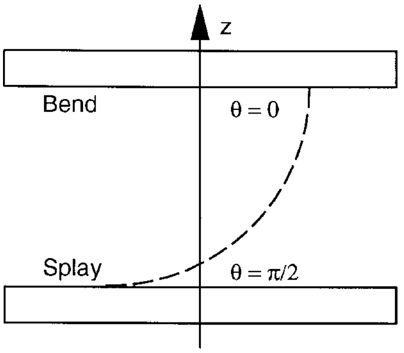

Figure 6. A splay–bend layer produced by hybrid boundary conditions (after Meyer [4]).

boundary conditions at the other. Solutions exist for equal constants, high splay constant and high bend constant.

The director must change in orientation by 90° from one plate to the other. The way that the angle varies depends on the ratio of the splay and bend elastic constants. If the elastic constants are equal, the director varies smoothly ($d\theta/dz$ is constant). If the splay constant is very much higher than the bend constant then all the splay distortion is spread between the plates, while the bend distortion is concentrated near to the homeotropic boundary. If the bend constant is the largest then the reverse occurs; the bend distortion being spread between the plates, while the splay is concentrated near to the homogeneous boundary. This behaviour is an example of a general rule: the higher the elastic constant for a particular distortion, the more spread out that type of distortion will be.

The analytical results for the variation of the angle of the director, θ_z, for two plates separated by a distance d are as follows.

For $k_{11} = k_{33}$:

$$\theta_z = \frac{\pi}{2}\left(1 - \frac{z}{d}\right) \tag{12}$$

For $k_{11} \gg k_{33}$:

$$\theta_z = \cos^{-1}\left(\frac{z}{d}\right) \tag{13}$$

For $k_{33} \gg k_{11}$:

$$\theta_z = \sin^{-1}\left(1 - \frac{z}{d}\right) \tag{14}$$

In deriving these solutions, Meyer assumed (reasonably) that the distortion would be two dimensional with the director remaining in the plane defined by the homeotropic and homogeneous boundary conditions and that the director orientation, θ_z is a function only of z.

By using the numerical technique, it has been possible to simulate this geometry in three dimensions. An advantage of this approach is that no assumptions are made as to the nature of the solutions. If a solution involving some twist distortion is favoured, then it is not precluded by the way the simulation is set up. Simulations were run from random initial conditions in the simulated annealing mode to anneal the system to its minimum energy state. Figure 7 shows the results of the simulations for the three situations of a high splay constant, equal constants and a high bend constant. It is clear that, when the splay constant is high, the splay distortion is spread out and that the bend distortion is concentrated near to the homeotropic boundary ($z = d$); when the bend constant is high the bend distortion is spread out and the splay distortion is concentrated near to the homogeneous boundary ($z = 0$); with equal constants the director varies smoothly from one boundary to the other.

A comparison between the analytical and the simulated results is plotted in figure 8 with $k_{11} \gg k_{33}$ being simulated by setting $k_{11} = 1$, $k_{22} = 1$ and $k_{33} = 0$; $k_{11} \ll k_{33}$ is simulated by setting $k_{11} = 0$, $k_{22} = 1$ and $k_{33} = 1$, and equal constants are simulated by setting $k_{11} = k_{22} = k_{33} = 1$. The agreement with the analytical results is excellent, giving further confidence in the numerical technique. The technique may be used to find solutions for any ratio of elastic constants. The solutions occupy the region bounded by the limiting cases shown in figure 7.

3.3. *Fréedericksz transition*

An additional test of the technique has been to simulate the Fréedericksz transition [19]. In the Fréedericksz transition, samples are typically constrained by two parallel plates. The surfaces of the plates impose either homeotropic or homogeneous boundary conditions which define the direction of alignment at zero applied field. By the application of a critical field the alignment begins to change from a monodomain aligned in the direction defined by the boundaries towards the direction favoured by the applied field. The onset of the transition involves only one type of distortion and so the critical field is dependent only on the elastic constant associated with that distortion. By suitable choice of geometry, all three distortions may be probed. For equal elastic constants, all three geometries should show the transition at the same critical field. Figure 9 shows a schematic of the three geometries.

It is simple to simulate the Fréedericksz transition using the numerical technique described here. The effect of a magnetic field is included via an additional energy term as shown in equation (15), where χ_a is the anisotropy in the diamagnetic susceptibility per unit volume, **H** is the field strength and **n** is a vector parallel to the director stored in a given cell.

$$E_{\mathrm{mag}} = \frac{1}{2}\chi_{\mathrm{a}}(\mathbf{H}\ \mathbf{n})^2 \tag{15}$$

The first test was to show that the transition occurred at the same applied field for each geometry. Figure 10 shows the variation of the angle of the director on the mid-plane of the simulation as a function of applied field strength for the splay geometry. The graphs for the twist and bend geometries are identical. According to theory (see for example [20]), the transition should occur at a field strength given by equation (16).

$$H_{\mathrm{c}} = \frac{\pi}{d}\left(\frac{k}{\chi_{\mathrm{a}}}\right)^{1/2} \tag{16}$$

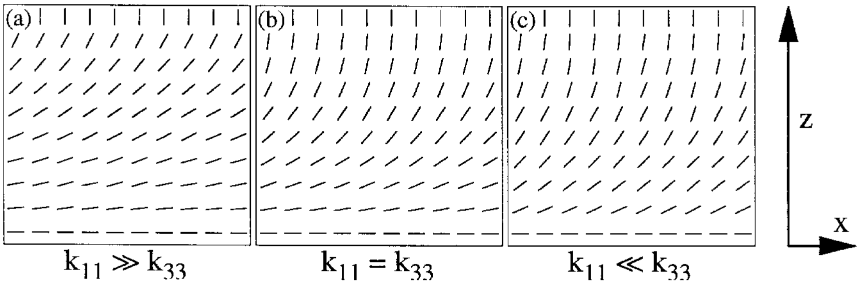

Figure 7. Minimum energy director fields for parallel plates with homogeneous boundary conditions at $z=0$, and homeotropic boundary conditions at $z=d$. The results shown are x-z slices through a three dimensional ($10\times10\times10$) simulation with fixed boundaries at $z=0$ and $z=d$ and periodic boundaries in the x and y directions. (*a*) Shows the variation of the director across the sample for a high splay constant; the splay distortion is spread out and the bend distortion is concentrated near the $z=d$ boundary. (*b*) Shows the variation for equal constants; the director varies uniformly. (*c*) Shows the variation for a high bend constant; the bend distortion is spread out and the splay distortion is concentrated near the $z=0$ boundary layer.

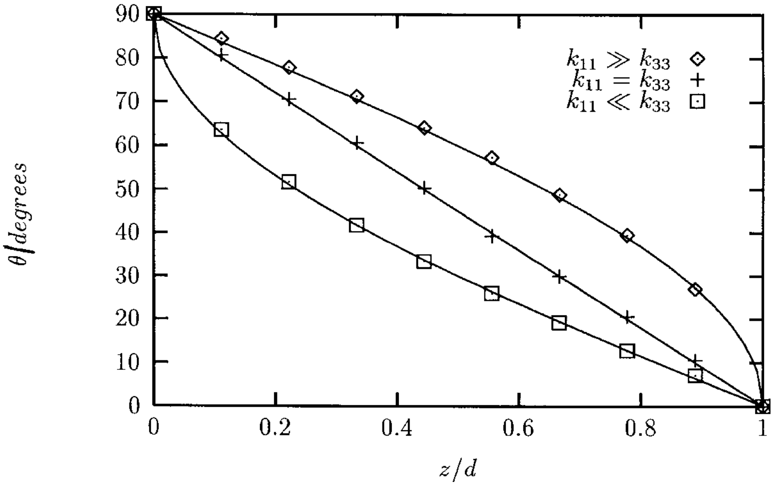

Figure 8. The actual variation of the director angle across the sample is plotted to compare simulated and analytical results. The lines represent the analytical results in each case while the points are the simulated values. In the simulation with $k_{11} \gg k_{33}$, k_{33} was actually set to zero; for the simulation with $k_{11} \ll k_{33}$, k_{11} was set to zero.

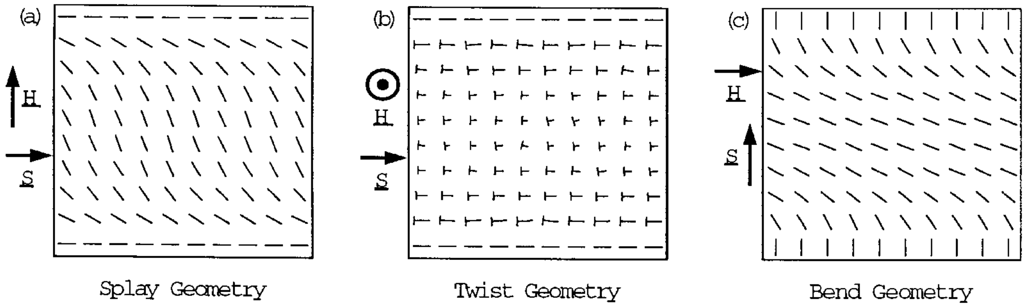

Figure 9. Diagrams showing the three geometries of the Fréedericksz transition. S is the direction of monodomain alignment imposed by the boundary conditions when there is zero applied field, H is the direction of the applied field. The diagrams show the variation of the director between the two plates for a field strength which is significantly higher than the critical field strength.

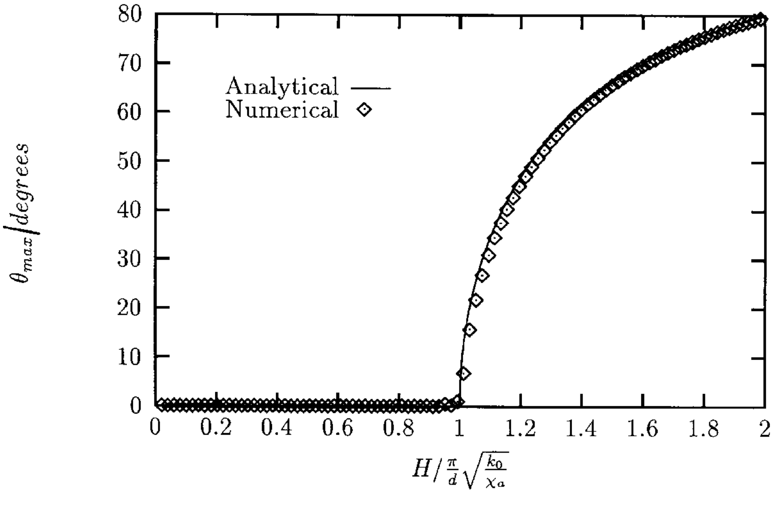

Figure 10. Plot of θ_{max}, the angle of the director on the mid-plane, versus **H**, the magnetic field strength, for the splay geometry with equal elastic constants, $k_{11}=k_{22}=k_{33}=k_0$. The simulation was performed using a $1\times1\times10$ lattice ($d=9d_0$). The actual values for k_0, d_0 and χ_a were set to unity in the simulation. Each data point involved a calculation of 64 000 Monte Carlo trials per cell at values of β increasing from 8 to 8×10^8. The graph shows excellent agreement between the simulated and analytical results; the transition occurs at the theoretical critical field. The curves for the twist and bend geometries are identical and have not been plotted.

where d is the separation of the plates and k is the relevant elastic constant. Figure 10 shows the transition occurring at exactly this field strength.

Once the critical field has been reached, further increase of the field will cause the director to turn further and further towards the field direction. Chandrasekhar [20] has calculated how the director on the mid-plane of the sample varies as a function of field strength. Figure 10 shows a comparison of the analytical results and the result of simulations using the numerical technique.

Of further interest are simulations where the elastic constants are changed with respect to each other. The onset of the splay transition should depend only on the value of the splay elastic constant and so should remain unaltered by any change in the bend constant. However once the director has begun to rotate towards the magnetic field, then the distortion will begin to involve some bend distortion and so the bend elastic constant will have an effect on the rotation of the director with increasing field. One would expect an increase in the bend constant to reduce the rotation of the director with increasing field. Figure 11 shows just such behaviour.

Having shown that the position of the splay transition is unaffected by changes in the value of the bend elastic constant, a further test is to show that the position of the splay transition *is* affected by changes in the value of the splay constant. Figure 12 shows that the position of the transition is proportional to the square root of the splay elastic constant as expected from equation (16).

Another test of the simulation was to determine what effect lattice size has on the transition. The theory of the

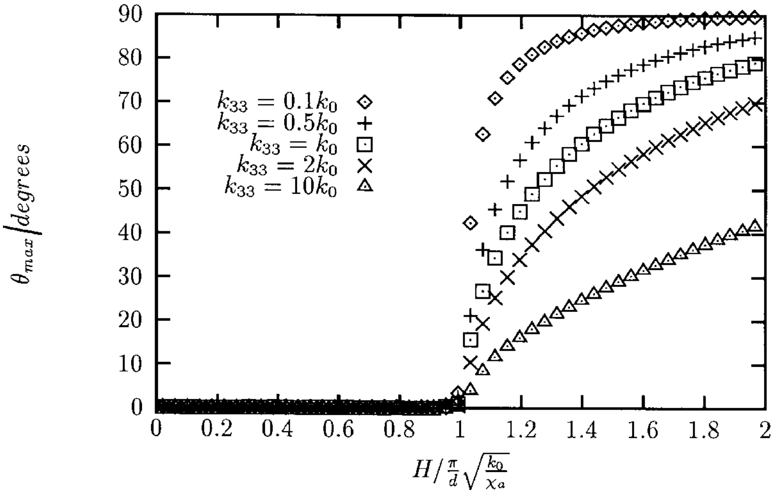

Figure 11. Graph showing the variation of θ_{max}, the director angle at the mid-plane, versus magnetic field strength, determined from the model. The five curves represent simulations run with the splay constant fixed at $k_{11}=k_0$ and varying bend constant. It is clear that while the onset of the transition is unaltered by the variation of the bend constant, for fields higher than the critical field, θ_{max} is strongly affected by the value of the constant. If the bend constant is high then the director is hindered from rotation towards the magnetic field. The simulations were run under the same conditions as used for figure 10.

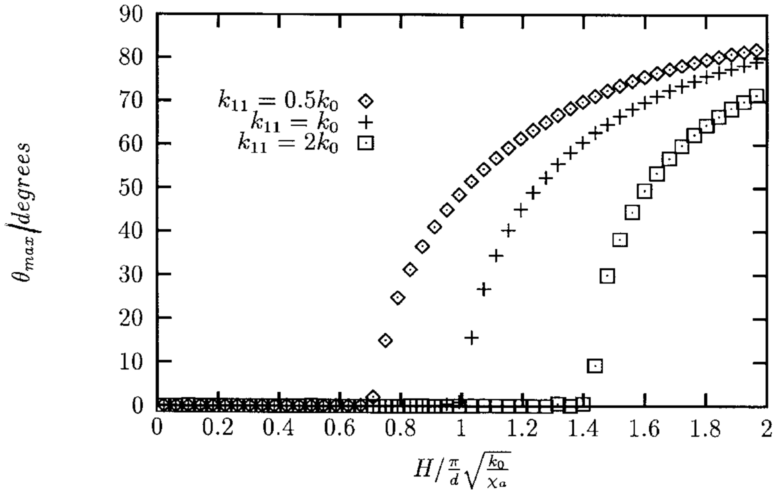

Figure 12. Graph showing the variation of $\theta_{\max}$, the director angle at the mid-plane, versus magnetic field strength in the splay geometry. The three curves represent simulations run with the bend constant fixed at $k_{33} = k_0$ and varying splay constant. The position of the transition changes as a result of the different splay constant. When the splay constant is halved, the critical field is multiplied by $(\frac{1}{2})^{\frac{1}{2}}$ whereas when the splay constant is doubled the critical field is multiplied by $2^{\frac{1}{2}}$. The simulations were run under the same conditions as used for figure 10.

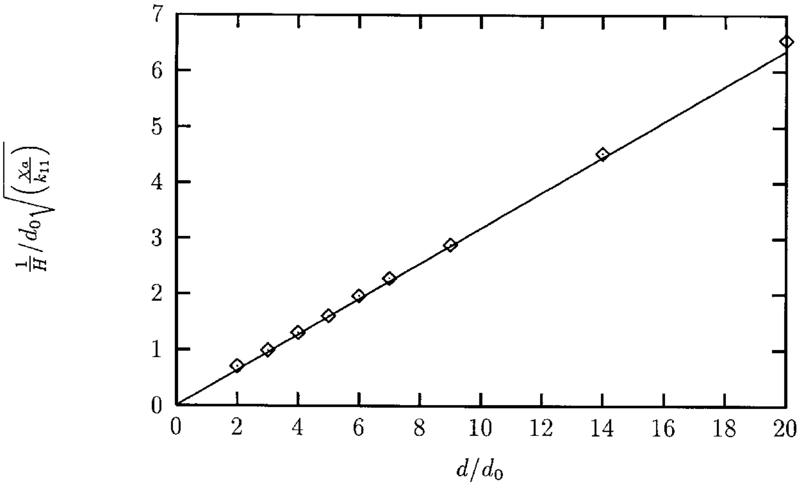

Figure 13. Relationship between the reciprocal of the critical field and the separation of the plates is a straight line. In the graph, d is the lattice size minus one and d_0 is the size of the lattice cells, arbitrarily assigned the value of 1 unit of length. It can be seen that down to very small values of d the straight line relationship is maintained.

Fréedericksz transition predicts that the critical field is proportional to the reciprocal of the space between the parallel plates. In the simulations here, this spacing is proportional to the number of lattice cells minus one in the direction with the fixed boundaries. Figure 13 shows the variation of the critical field with the reciprocal of the planar spacing. It can be seen that the straight line behaviour is maintained down to simulations of just 3 cells! This behaviour is accounted for by the fact that the onset of the transition is the point at which the director in the mid-plane just starts to rotate away from the monodomain alignment imposed by the boundary cells. At this point the angle of rotation is very small and so even for small lattice sizes the numerical approximations hold good.

4. Simulation of the bulk

The technique has been used to study the evolution of textures and how the shapes of the defects which are present during the evolution vary with different elastic constants. In particular, simulations have been run with the elastic constants in the ratio thought to occur in liquid crystalline polymers.

In order to probe the bulk, simulations have been performed with periodic boundary conditions. If the simulations are run for sufficient time then the microstructures will anneal to a monodomain with all the directors lying at the same orientation. However, if the simulations are stopped at an earlier time, then states are found where all the high energy distortions have annealed out leaving a network of disclinations. The nature of the microstructure which is revealed depends strongly on the elastic constants inserted into the simulation.

In order to obtain quantitative information about the nature of the defects which occur in simulations, algorithms have been devised to analyse the data produced from simulations. Before presenting results from simulations, a description of these ‘topological probes’ is included.

4.1. *Topological probes*

The first probe used identifies $\frac{1}{2}$ strength disclination lines and is based on an algorithm derived by Zapotocky *et al.* [10]. Their algorithm is two dimensional, but is extended simply to three dimensions by repeating for sets of four cells in the *x*-*y* plane, the *y*-*z* plane and the *z*-*x* plane. In essence, the algorithm involves searching around all sets of four cells forming a 2×2 square and checking for a contained disclination. A disclination is found if, when stepping around the set of four cells in a clockwise direction, the director changes its orientation by 180°. Figure 14(*a*) shows an example of a strength $\frac{1}{2}$ twist disclination contained by a set of four cells. Once the location of the cores of disclinations have been identified as a series of sorted points, then an attempt is made to distinguish between wedge and twist disclinations. The characteristic which distinguishes these types of disclinations is the angle between the rotation vector, $\boldsymbol{\Omega}$, and the direction of the disclination line, $\mathbf{L}$. In this paper, this angle is termed the characteristic angle of the disclination, α. An approximate direction for the rotation vector, which is the axis of the rotational distortion around the disclination line [21, 22], is found by adding the vector cross products formed from each pair of the four directors surrounding the disclination core. Given that the path of the disclination line has been determined as a sorted sequence of points in three dimensions, an approximation to the direction of the line at any point may be taken as the vector from the previous point along the line to the next point along the line as shown in figure 14(*b*). The angle between the rotation vector, $\boldsymbol{\Omega}$, and the disclination line, $\mathbf{L}$, is found. If the characteristic angle α is 0°, the disclination is pure wedge in nature; if the angle α is 90°, then the disclination is pure twist in nature; if the angle α is between these values, then the disclination is of mixed nature. A shortcoming of the current algorithm is that it is not able to determine the sign of the disclination. This is because the algorithm only finds the acute angle between the direction of the disclination line and the rotation vector. To distinguish between $+\frac{1}{2}$ and $-\frac{1}{2}$ wedge disclinations it is necessary to determine whether the rotation vector is parallel to the disclination line ($+\frac{1}{2}$) or antiparallel to the disclination line ($-\frac{1}{2}$).

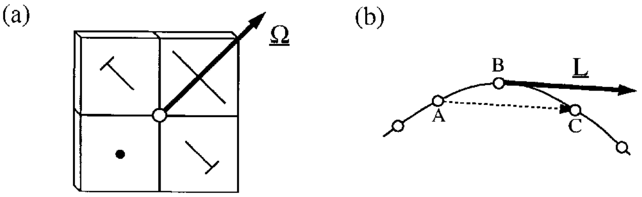

Figure 14. (*a*) All sets of four cells forming a 2×2 square are checked using the algorithm described by Zapotocky *et al.* [10] to find disclinations. If a disclination is found then the coordinates of the site are recorded. When a disclination is found its rotation vector is determined by taking the cross product of each pair of directors around it and summing the resultant vectors. In the diagram, all the directors lie in a plane and the rotation vector, Ω, is the normal to this plane. (*b*) Having found the coordinates of all the disclination sites, the sites are sorted such that they form a continuous disclination line (or lines). The direction of the line at any point is estimated by taking the vector from the previous site along the line to the next site along the line. In the diagram, the direction of the disclination line at site B is taken to be the vector from site A to site C. The character of the disclination line at each site is determined by finding the angle between the rotation vector and the direction of the line.

A second probe identifies escaped strength 1 disclination lines. This algorithm operates by considering a two dimensional square circuit. The projection of the directors onto the two dimensional plane are found and as the circuit is traversed the total angle through which the projected director varies is found. If this angle is 360°, then either an escaped strength 1 defect, or a pair of strength $\frac{1}{2}$ defects is contained within the circuit. Various sizes of circuit may be used. If a 2×2 square is used then strength 1 disclinations may not be distinguished from a monodomain. The smallest circuit which can be used is a 3×3 square. Sizes up to 7×7 have been considered, but the best results seem to be obtained with a 4×4 circuit. If smaller circuits are used then not all escaped lines are found. If larger circuits are used then many circuits will find the same escaped line and the location of the line cannot be determined with any precision. Also, the likelihood of finding pairs of $\frac{1}{2}$ strength disclinations of equal sign is higher for larger circuits. The operation of the circuits is illustrated in figure 15.

4.2. *Simulation for equal constants*

With equal elastic constants the microstructures look similar to the simulation outputs from various other techniques. Figure 16 shows a slice through a simulation run for this condition. However, it is interesting to note the presence of escaped strength -1 lines which have not in general been seen in earlier simulations, and figure 17 shows an enlargement of the escaped -1 line shaded in figure 16. The occurrence of escaped -1 lines probably reflects the correct handling of splay–splay compensation in the new algorithm, for such a line is an example of a splay–splay compensated structure as discussed in §2.3. Earlier numerical techniques will treat this geometry as a high energy state rendering it less likely to occur, while in this improved approach it actually has zero energy down the centre. A fuller treatment including the k_{24} term is required to determine whether escaped -1 lines are really likely to prevail in small molecule microstructures.

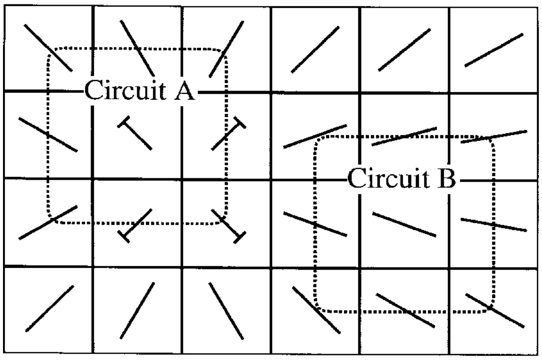

Figure 15. To investigate the occurrence of escaped disclination lines of unit strength, circuits are performed around the projections of the directors onto the *x*-*y* plane, the *y*-*z* plane and the *z*-*x* plane. In the diagram, both circuits are around 3 × 3 squares of cells. Circuit A encloses an escaped strength +1 disclination; when circuit A is traversed, the orientation of the projection of the director changes by 360°. Circuit B does not enclose a defect; when circuit B is traversed the orientation of the projection of the director remains unchanged. Circuits may be performed around larger squares of cells, but it is more than likely that an escaped strength 1 disclination will be confused with two $\frac{1}{2}$s of the same sign, and also that the position of the axis of the defect will not be known with as much precision.

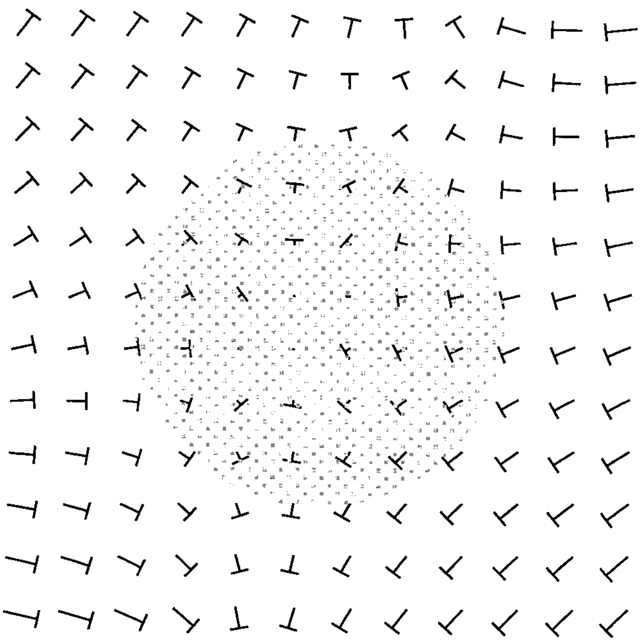

Figure 17. A close up of the escaped −1 disclination line highlighted in figure 16. Comparison with figure 3 confirms that the feature is indeed an escaped −1 line and that it is thus a region of splay–splay compensation.

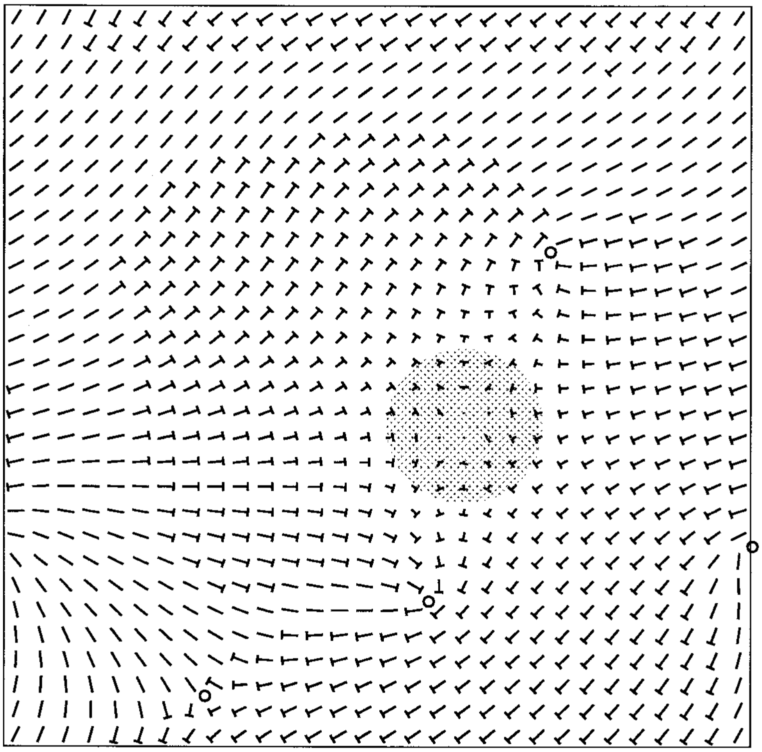

Figure 16. Results from a simulation performed on a 30 × 30 × 30 lattice with periodic boundary conditions. The simulation was run with equal constants, $k_{11}=k_{22}=k_{33}=1$, and with $\beta=30$; it was run for 40 000 Monte Carlo trials per cell. The diagram shows an *x*-*y* slice through the model; it shows four $\frac{1}{2}$ strength disclinations indicated by small circles and an escaped strength −1 disclination in the shaded region.

The equal constants simulations show $\frac{1}{2}$ strength disclination lines which reduce in length as the simulations proceed. The character of the disclinations is equally portioned between wedge and twist types. To illustrate the difference in character a colour coding has been used. For those disclination lines with a characteristic angle of less than 30° between the line and the rotation vector, implying a predominantly wedge type, the colour blue is used; for disclinations with a characteristic angle of greater than 60°, implying a predominantly twist type, the colour red is used; for lines with a characteristic angle of between 30° and 60°, implying a mixed type, the colour green is used. Figure 18 shows a single $\frac{1}{2}$ strength disclination line of varying character which snakes its way through the periodic simulation box and several escaped strength -1 lines. With periodic boundary conditions, the simulation box tessellates and, in fact, the sections of strength $\frac{1}{2}$ line seen in the figure are all sections of periodic copies of a single line which forms a closed loop. This condition implies that sections of the line will be experiencing the distortion fields around other sections of the same line. The longest of the escaped strength -1 lines clearly connects two sections of the strength $\frac{1}{2}$ line. Topologically, it is impossible for a disclination line to terminate within the bulk. It may either close on itself to form a loop, terminate on a surface or form a junction with another disclination line. By performing computer simulations, it is possible to examine what is occurring in the bulk far more readily than in experiments. It is possible to look at the structure of the disclinations at the junction between a strength $\frac{1}{2}$ line and an escaped -1 line. The longer of the strength -1 lines in figure 18 does not meet the strength $\frac{1}{2}$ line at a convenient angle to the underlying lattice for analysis, so one of the shorter sections is considered. It is worth noting the fact that disclinations do not always meet at convenient angles to the lattice of cells; this is actually reassuring since it implies that the lattice is not imposing special directions along the coordinate axes.

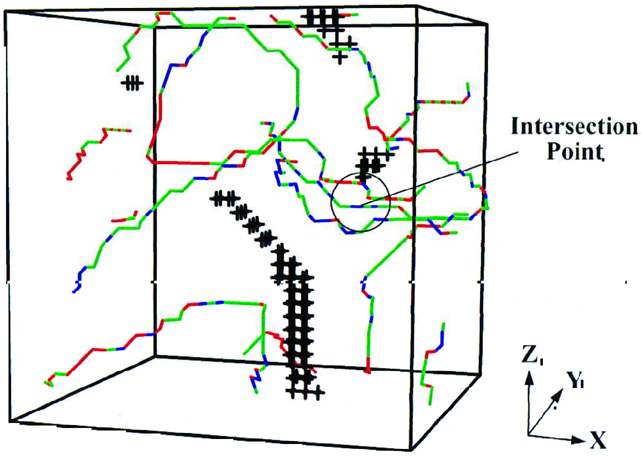

Figure 18. A strength $\frac{1}{2}$ disclination line, shown in colour, with escaped -1 lines, shown as black crosses, running from one part of the $\frac{1}{2}$ line to another. At points where strength -1 lines meet the strength $\frac{1}{2}$ disclination line the character of the disclination changes abruptly. The intersection indicated is examined in more detail in figure 19. The results are from the same simulation as shown in figure 16.

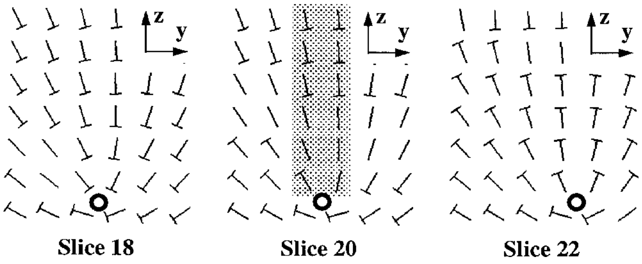

Figure 19. A closer examination of y-z slices through the same simulation as in figure 18 reveals a change in the character of the strength $\frac{1}{2}$ line from one side of an escaped strength -1 line to the other. In the diagrams, the strength $\frac{1}{2}$ disclination is directed straight out of the page, passing through slices 18, 19, 20, 21 and 22 in turn. The escaped strength -1 line (shaded) lies in the plane of the diagrams in slice 20. As can be seen, the rotation vector in slice 18 is in approximately the $(-1\ 0\ 1)$ direction, while the rotation vector in slice 22 is in approximately the $(1\ 0\ 1)$ direction. Since the disclination line continues in the positive x direction there is the implication of a change in the character of the disclination line from one side of the escaped -1 line to the other. (Figure 20 shows a schematic of the situation viewed on the z-x plane.)

By stepping through the simulated volume one layer at a time it is possible to observe the character of the $\frac{1}{2}$ strength disclination line on either side of the junction with the escaped strength -1 line. Figure 19 shows three such layers, one to one side of the junction point, one coincident with the junction and one to the other side of the junction point. As the $\frac{1}{2}$ strength line passes the junction with the escaped -1 line, the rotation vector changes direction suggesting a change in the character of the $\frac{1}{2}$ strength disclination line. Figure 20 shows a schematic of the way the rotation vector changes from one side of the junction to the other. The $\mathbf{\Omega}$ vector of the strength $\frac{1}{2}$ disclination, and the distortion field, associated with it, is rotated by π about the -1 axis.

4.3. *Varying the twist constant*

Anisimov and Dzyaloshinskiĭ [23] have deduced that when the elastic constants are not equal, the type

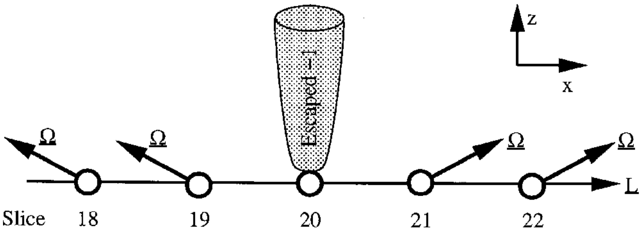

Figure 20. A schematic showing the relationship between the rotation vectors and the disclination line on either side of the escaped -1 line shown in figure 19.

of strength $\frac{1}{2}$ disclination lines which are stable in three dimensions depends on the values of the elastic constants. They quote the following two cases:

if $k_{22} > \frac{1}{2}(k_{11} + k_{33})$, the planar wedge lines of strength $\pm\frac{1}{2}$ are stable;
if $k_{22} < \frac{1}{2}(k_{11} + k_{33})$, the twist lines of strength $\pm\frac{1}{2}$ are stable.

Simulations have been performed for both these situations, with a high twist elastic constant and with a low twist elastic constant. The disclination lines which occur are very different in each case. For a low twist elastic constant, as shown in figure 21 the disclinations are predominantly twist (coloured red) in character. For a high twist elastic constant, as shown in figure 22 the disclinations are predominantly wedge (coloured blue) in character. Both findings are in accord with the theoretical predictions, although neither pure wedge is eliminated for a low twist constant nor pure twist for low splay/bend constants.

A more quantitative means of comparing the equal constants simulations, the high twist and the low twist constant simulations is to analyse the distribution of characteristic angles of the disclinations which occur. Figures 23(*a*) to 23(*c*) are histograms showing the distribution of disclination types in simulations. It is interesting to note that when the twist constant is low, almost all the disclination lines are of twist character, but that when the twist constant is high, there is a broader distribution of types peaked at the wedge (0°) end. This 'skewing' of the distribution represents the fact that for a given rotation (Ω) vector, a wedge disclination requires the line to be parallel to Ω, whereas for a twist disclination it is normal to Ω which provides many more possible orientations.

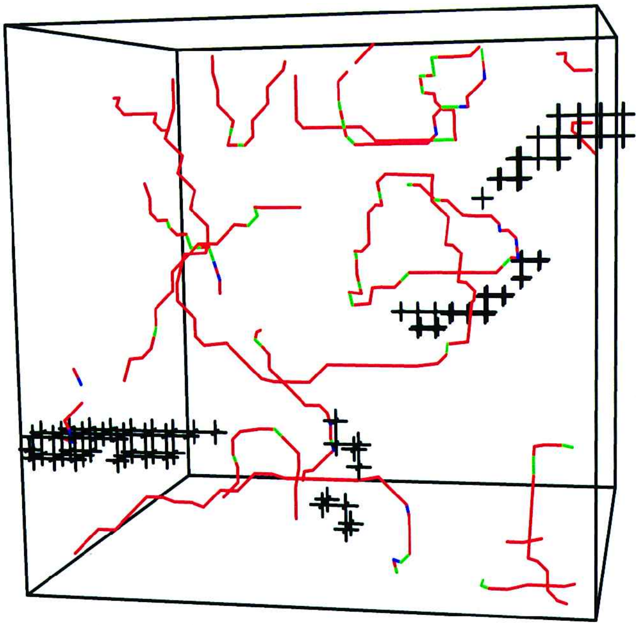

Figure 21. Results from a simulation performed on a $30 \times 30 \times 30$ lattice with periodic boundary conditions. The simulation was run with a low twist constant, $k_{11} = 1$, $k_{22} = 0{\cdot}1$, $k_{33} = 1$, and $\beta = 30$; it was run for 40 000 Monte Carlo trials per cell.

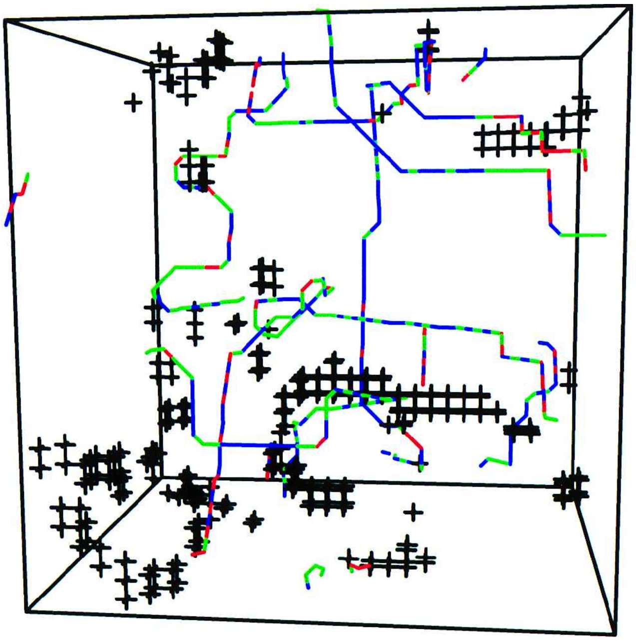

Figure 22. Results from a simulation performed on a $30 \times 30 \times 30$ lattice with periodic boundary conditions. The simulation was run with a high twist constant, $k_{11} = 0{\cdot}1$, $k_{22} = 1$, $k_{33} = 0{\cdot}1$, and $\beta = 30$; it was run for 40 000 Monte Carlo trials per cell.

4.4. *High splay constant—the polymeric case*

The primary goal of this work has been to model microstructure in liquid crystalline polymers. In this section, results from a simulation run with elastic constants in the ratio thought to be reasonable for main-chain thermotropic LCPs are presented. The elastic constants used are in the ratio $k_{11} : k_{22} : k_{33} = 100 : 1 : 10$ and a typical model is shown in figure 24 for 40 000 Monte Carlo trials per cell. Almost all of the disclinations are twist in character. Figure 25 shows a slice through the simulation after 5000 Monte Carlo trials per cell. The microstructure is very different from the equal constants simulation in §4.2. It is apparent that there is considerable twist distortion present—consistent with the low twist constant inserted into the simulation. In particular, the escaped strength 1 disclinations which are observed in these simulations are most often of the twist-escaped strength +1 variety. Such structures have zero splay distortion and so are indeed likely to be favoured when the splay constant is high. Such twist-escaped lines are observed experimentally in liquid crystalline polymers using fractography [14].

Another interesting feature of simulations run with a high splay constant and low twist constant is the tendency for layering to occur. Figure 26 is a section which happens to show the layers clearly; they form with twist distortion between the layers. It should be stressed that although the structures are reminiscent of cholesteric textures, there is no chirality present in the free energy expression and the twist is equally likely to be clockwise or anticlockwise. This layering occurs because any deviation from the layer would involve splay distortion which is prohibited by the high splay constant. Within the layers there is bend distortion and also associated splay. The layering would account for the micaceous texture often seen in thermotropic LCPs [24, 25].

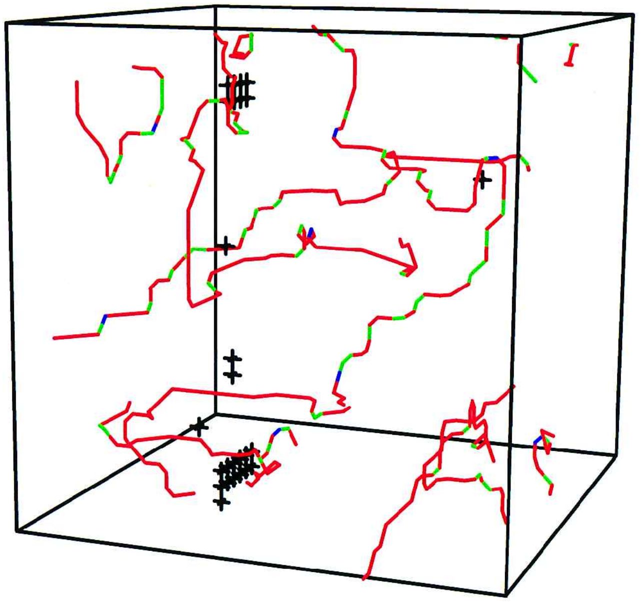

Figure 24. Results from a simulation run on a $30 \times 30 \times 30$ lattice with periodic boundary conditions. The simulation was run with elastic constants in the ratio thought to occur in liquid crystalline polymers: $k_{11} = 100$, $k_{22} = 1$, $k_{33} = 10$. The value of β was set to 30 and the simulation was run for 40 000 Monte Carlo trials per cell. As can be seen, the disclinations are mainly twist in nature.

5. Summary

In this paper we have presented a numerical technique for predicting microstructure in nematic liquid crystals. It is an advance over previous techniques in that it differentiates between the three distortions of splay, twist

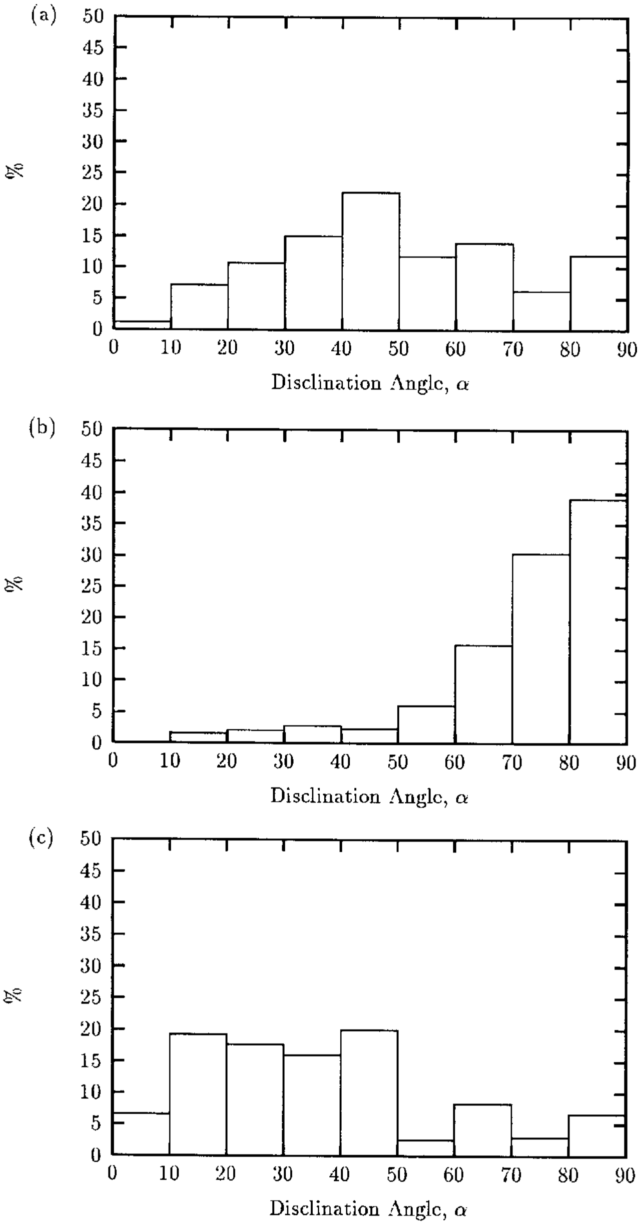

Figure 23. Distribution of disclination types as characterized by the angle between the disclination line and the rotation vector. (*a*) For the simulation in figure 16: this simulation was run with equal elastic constants. The disclinations are predominantly of mixed character; there is no preference for wedge or twist character disclinations for the situation of equal elastic constants. The average characteristic angle is 49°; the number of disclination sites is 432. (*b*) For the simulation in figure 21: this simulation was run with a very low twist elastic constants and the distribution shows the majority of the disclinations had characteristic angles above 45° indicating they are of twist or predominantly twist character. The average characteristic angle is 73°; the number of disclination sites is 434. (*c*) For the simulation in figure 22: this simulation was run with a very high twist elastic constant and the distribution shows the majority of the disclinations had characteristic angles below 45° indicating they are of wedge or predominantly wedge character. The average characteristic angle is 37°; the number of disclination sites is 436.

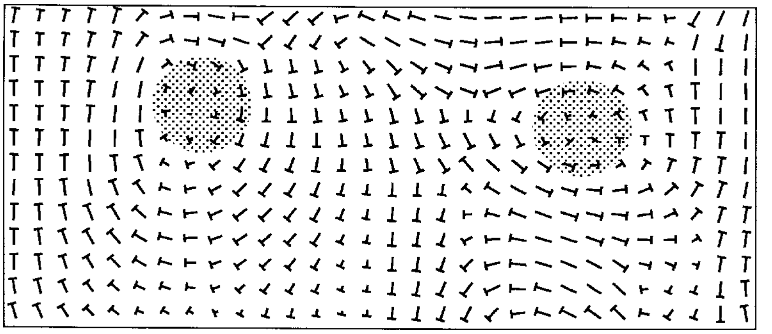

Figure 25. Part of a section through the simulation shown in figure 24 after 5000 Monte Carlo trials per cell. Note in particular the twist-escaped strength +1 lines which are shown shaded. Such 'swirls' are common in simulations run with a high splay elastic constant, since twist-escape of a +1 (bend only) disclination occurs without splay distortion.

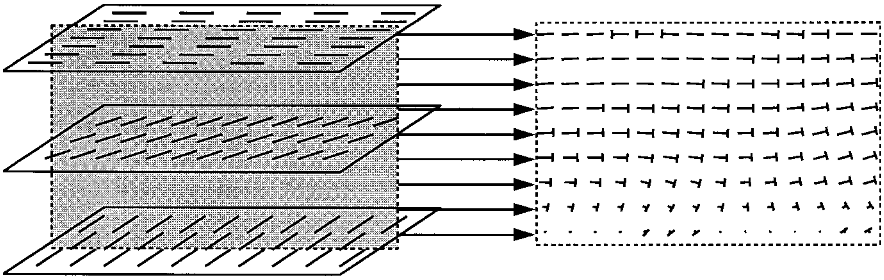

Figure 26. Part of another section through the simulation shown in figure 24 showing layering. The simulations run with a high splay constant and low twist constant often show a degree of layering with twist distortion between the layers and little registry from one layer to the next. In order for the director to deviate from such a layered structure it would have to introduce splay distortion which is highly unfavourable.

and bend and includes splay–splay compensation as a natural consequence of the calculation of the divergence of the director field in three dimensions.

The calculation of the splay, twist and bend energies for a set of predefined geometries—the Poincaré point singularities—agrees with analytical results. One of the point defects in particular, the Col defect, has a region of splay–splay compensation and the correct determination of the distortions for this case is evidence for the inclusion of splay–splay compensation.

The technique may be used to find director fields which minimize the Frank free energy for given boundary conditions.

It is simple to include the effect of an aligning field into simulations and with the inclusion of such a field the Fréedericksz transition has been simulated. The critical field is correctly predicted for each geometry and the variation of the director with higher fields also agrees with analytical theory.

The technique has been used to simulate the bulk by imposing periodic boundary conditions. In this mode, the global minimum will be a monodomain regardless of the elastic constants applied. However, if simulations are halted before the monodomain solution is found, then networks of disclination lines are found. The location and character of the lines has been determined by the use of 'topological probes'.

A number of situations have been considered: equal elastic constants, high twist constant, low twist constant and elastic constants in the ratio considered to occur in liquid crystalline polymers. With equal elastic constants, the character of the strength $\frac{1}{2}$ disclinations seen in simulations varies between the limiting case of pure wedge type and pure twist type. With a low twist constant, predominantly twist disclinations are seen and with a high twist constant, predominantly wedge disclinations.

Strength 1 disclination lines are topologically unstable with respect to escape in the third dimension. Escaped strength 1 defects are seen in all the simulations, but the type of line varies dependent on the elastic constants. With equal elastic constants the lines are escaped -1 lines. These may be unrealistically favoured since they exhibit saddle-splay distortion which is not assigned an energy in the simulations.

As stated earlier, the primary goal of this work has been to simulate microstructure in liquid crystalline polymers by applying elastic constants in the ratio which occurs in these materials. Simulations have been performed with the elastic constants in the ratio $k_{11}:k_{22}:k_{33} = 100:1:10$. The following conclusions have been drawn:

(a) Strength $\frac{1}{2}$ disclination lines in liquid crystalline polymers will be predominantly twist in character as a result of the low twist elastic constant. This conclusion is supported to some extent by recent experimental studies by Gieger [26] who has observed LCPs in shear flow.

(b) Strength 1 disclination lines in liquid crystalline polymers will be of the twist-escaped strength $+1$ variety. This conclusion is supported by the fact that such structures are free of any splay distortion which is prohibited by the high splay constant. Experimental observation of fracture surfaces by the authors [22] has revealed features which are certainly consistent with twist-escaped strength $+1$ lines.

(c) A degree of layering as a consequence of the high splay constant is predicted for liquid crystalline polymer melts. Put another way, the layering which gives rise to the micaceous fracture behaviour of mouldings and is also apparent in the textures [27] is seen as a direct consequence of the high splay constant of the thermotropic polymer.

Further work is required to determine whether saddle-splay distortion is important in liquid crystalline polymers. The reason that the splay constant is high in polymeric liquid crystals, the lack of chain ends, is not applicable to the case of saddle-splay. For pure splay, the only way a divergence can be supported without violating a continuity of material is to have chain ends (or molecular hairpins) to fill the gaps. However, if splay on one plane is compensated by splay in the opposite direction on a perpendicular plane then the problem of the lack of chain ends is alleviated: any part of a chain splaying in an opposite direction may fill the gaps due to the splay on the perpendicular plane. It thus seems reasonable to expect that the k_{24} or saddle-splay constant will have a magnitude more like the twist constant, which reflects only the reluctance of the chain units to be misaligned, rather than the splay or bend constants which are higher as a result of the length (few ends) and comparative rigidity of mesomorphic molecules.

References

[1] Donald, A. M., and Windle, A. H., 1992, *Liquid Crystalline Polymers* (Cambridge University Press).

[2] Oseen, C. W., 1933, *Trans. Faraday Soc.*, **29**, 883.

[3] Frank, F. C., 1958, *Discuss. Faraday Soc.*, **25**, 19.

[4] Meyer, R. B., 1982, *Polymer Liquid Crystals*, edited by W. R. Krigbaum, A. Ciferri, R. B. Meyer (New York: Academic Press), Chap. 6.

[5] De'Nève, T., Kléman, M., and Navard, P., 1995, *Liq. Cryst.*, **18**, 67.

[6] Kilian, A., and Hess, S., 1989, *Z. Naturforsch*, **44a**, 693.

[7] Kilian, A., and Hess, S., 1990. *Liq. Cryst.*, **8**, 465.

[8] Chuang, I., Durrer, R., Turok, N., and Yurke, B., 1991, *Science*, **251**, 1336.

[9] Bedford, S. E., Nicholson, T. M., and Windle, A. H., 1991, *Liq. Cryst.*, **10**, 63.

[10] Zapotocky, M., Goldbart, P. M., and Goldenfeld, N., 1995, *Phys. Rev. E*, **51**, 1216.

[11] Metropolis, N., Rosenbluth, A. W., Rosenbluth, M. N., Teller, A. H., and Teller, E., 1953, *J. chem. Phys.*, **21**, 1087.

[12] Allen, M. P., and Tildesley, D. J., 1987, *Computer Simulation of Liquids*, 1st Edn (Oxford: Oxford University Press).

[13] Lebwohl, P. A., and Lasher, G., 1972, *Phys. Rev. A*, **6**, 426.

[14] Hobdell, J. R., and Windle, A. H., 1995, *J. Chem. Soc. Faraday Trans.*, **91**, 2497.

[15] Gruhn, T., and Hess, S., 1996, *Z. Naturforsch*, **51a**, 1.

[16] Bedford, S. E., and Windle, A. H., 1993, *Liq. Cryst.*, **15**, 31.

[17] Poincaré, H., 1886, *Journal de Mathématiques*, **2**, 151.

[18] Hobdell, J. R., and Windle, A. H., 1995, *Liq. Cryst.*, **19**, 401.

[19] Fréedericksz, V., and Zolina, V., 1933, *Trans. Faraday Soc.*, **29**, 919.

[20] Chandrasekhar, S., 1992, *Liquid Crystals*, 2nd Edn (Cambridge University Press), p. 99.

[21] Kléman, M., 1983, *Points, Lines and Walls* (Chichester: John Wiley and Sons).

[22] Windle, A. H., Assender, H. E., and Lavine, M. S., 1994, *Philos. Trans. R. Soc. London*, **348**, 73.

[23] Anisimov, S. I., and Dzyaloshinskiĭ, I. E., 1973, *Sov. Phys. JETP*, **36**, 774.

[24] Bedford, S. E., and Windle, A. H., 1990, *Polymer*, **31**, 616.

[25] Baer, E., Hiltner, A., Weng, T., Sawyer, L., and Jaffe, M., 1990, *Abstr. Pap. Am. chem. Soc.*, **189**, 22-PMSE.

[26] Geiger, K., 1996, *Appl. Rheol.*, **6**, 172.

[27] Blundell, D. J., Chivers, R. A., Curson, A. D., Love, J. C., and Macdonald, W. A., 1988, *Polymer*, **29**, 1459.